Temperature influence on $Ti_3C_2T_x$ lines printed by aerosol jet printing

Michela Borghetti[a,*], Mauro Serpelloni[a], Emilio Sardini[a], Dahnan Spurling[b], Valeria Nicolosi[b]

[a] Dep. of Information Engineering, University of Brescia, Brescia, Italy
[b] CRANN and AMBER, School of Chemistry, Trinity College Dublin, Dublin, Ireland

ARTICLE INFO

Keywords:
MXene
Aerosol jet printing
Polymer substrate
Temperature dependence
Geometrical characterization

ABSTRACT

Aerosol jet printing (AJP) is a promising printing technology for fabricating sensors and electronics, due to its high flexibility in ink and substrate selection. Indeed, inks suitable for AJP can differ in morphology (2D and 3D nanoparticle, nanoflake, nanosheet, etc.), in electrical properties (conductive, semiconductive, insulating, etc.), or in additional advanced features (biocompatibility, stretchability, etc.). Inks can be deposited on planar, or complex 3D surfaces, which can be made of a variety of materials. $Ti_3C_2T_x$, a MXene, is a prominent 2D material, and is considered a promising material for energy storage electrodes and sensing elements due to its good stability and electrical conductivity. In this work, we propose a fabrication process based on AJP to print $Ti_3C_2T_X$ ink on PET-based sheets and we analyze the morphology (width and thickness) and the resistance by changing the number of overlaid printed layers (N_{layers}) and the pattern. The results from the morphological analysis and resistance measurements indicate uniform deposition and good repeatability using AJP, regardless of N_{layers} and the geometry of the printed pattern (thin lines, serpentine, long lines). Finally, for the first time, we estimate the temperature effects on the resistance of pure $Ti_3C_2T_X$ printed lines. For example, in the range − 10–60 °C and in the range 20–120 °C the resistance of $Ti_3C_2T_X$ printed on PET-based sheet increases by 13% and 20%, respectively. We also deposit different types of conformal coating to protect the printed layers from oxidation.

1. Introduction

In recent years, printing technologies have attracted interest from both the scientific community and manufacturers for the fabrication of novel electronics [1], sensors [2–5], actuators [6,7], and energy storage devices [8–10]. Flexibility, reduction of material wastage, and low fabrication costs are some of the main benefits of using these printing technologies [11], such as screen printing [12], inkjet printing (IJP) [13], and aerosol jet printing (AJP) [14]. Another attractive feature of printing technologies is the ability to deposit a wide variety of inks with different rheological, electrical, optical, and mechanical properties, giving a broad range of inks suitable for the substrate and specifications of the final application [15]. Unlike traditional micro- and nano-fabrication techniques such as photolithography, printing technologies can print biodegradable, biocompatible, or transparent inks on flexible or stretchable substrates, such as textiles, polymers, and paper [16]. For this reason, wearable devices [17], e-skin [18], organic electronics [19], and biodegradable electronics [20] are the main applications for printing technologies. AJP is an innovative and powerful contactless printing technology for fabricating sensors and electronics. The AJP system involves the deposition of functional inks atomized into an aerosol gas by an ultrasonic or pneumatic atomizer according to a Computer Aided Design (CAD) pattern. A carrier gas, usually nitrogen, reduces the ink into small droplets and transports the generated aerosol, which then passes into the virtual impactor, removing low-inertia droplets from the aerosol. The aerosol flow is transferred to the deposition head and is focused towards the substrate with an annular sheath generated by a secondary gas flow. Compared to other printing technologies such as IJP, AJP reduces the incidence of nozzle clogging and ink volume, and it can deposit inks with large range of viscosities (0.5–2000 cP). Furthermore, patterns printed by AJP can reach resolutions of 10 μm, while the feature size of IJP is higher than 30 μm [21]. Thus, it is possible to use inks with different rheological and electrical properties with only small hardware or software changes [22,23]. For example, Williams et al. [24] proved the multi-material printing capabilities of AJP by depositing proteins and silver nano-wires without removing the substrate from the printer. In [25], a silver nanoparticle ink and UV-curing adhesive used as dielectric ink were printed by AJP equipped with a pneumatic atomizer. With

* Correspondence to: Dep. of Information Engineering, University of Brescia, via Branze 38, Brescia, Italy.
E-mail addresses: michela.borghetti@unibs.it (M. Borghetti), mauro.serpelloni@unibs.it (M. Serpelloni), emilio.sardini@unibs.it (E. Sardini), spurlind@tcd.ie (D. Spurling), nicolov@tcd.ie (V. Nicolosi).

stand-off offsets between nozzle and substrate of 1–5 mm, AJP can be used to easily functionalize 2D and 3D surfaces for fabricating printed electronics and smart devices with low contamination, even when the complex surfaces are not reachable by physical nozzles [22]. AJP enables printing electronics on conformal and complex 3D surfaces with relatively simple 3-axis motion systems thanks to its consistent and focused aerosol jet, which does not need to be perpendicular to the surface [26]. Ink deposition by AJP is possible on almost any substrate geometry with more complex articulation and motion controls. For this reason, AJP can be combined with other additive manufacturing technologies, such as stereolithography [27] to enable the fabrication of smart devices on ready-to-use objects, lowering the production costs of prototypes [28]. AJP can be also considered as a 3D printing technology since the high flexibility of AJP concerning the ink formulation facilitates the printing of 3D microstructures [29–31]. For example, in [32] solenoid inductors with a solid core (polymer-core, iron-core, and ferrite-core) were fabricated by using AJP. The core volume was sliced up in a several sublayers of equal thickness, which were printed in a manner typical of standard 3D printing methods, and the silver ink was deposited over the cover to print the windings.

AJP is also a promising technology for depositing functional inks based on 2D materials in a controlled manner and for printing complex patterns. Recent advances in 2D materials including graphene [33–35], and MXenes [36–38] have pushed the adoption of printed electronics and the development of functional inks preserving the extraordinary electronic and optical properties of 2D crystals. For example, the most promising applications of such 2D materials are optoelectronic devices and energy storage devices [39]. MXenes are a new family of 2D crystalline metal carbides, nitrides, and carbonitrides that have attracted attention for their excellent mechanical, physical, and chemical properties. [40] For example, MXenes can be easily dispersed in aqueous solutions, exhibit good metallic conductivity [41], and have similar structure and properties to graphene while being relatively cheap to produce [42]. For this reason, MXene materials could be used in many different applications such as energy storage, electromagnetic interference shielding, strain sensors, gas sensors, and biosensors. Starting from the precursor MAX (where M is an early transition metal, A is an A group element, and X is C or N), the A-element is selectively etched from the layered MAX phase, and M atoms become the new surface of the bare MXene monolayer. Although more than 70 MAX phases have been reported in the literature [43], $Ti_3C_2T_x$ (T being O, OH or F surface terminations) is the most explored material because it is relatively stable, easily synthesized, and single nanosheets are micrometers in width but less than a nanometer in thickness. $Ti_3C_2T_x$ has been proved a promising material for developing supercapacitor electrodes; lithium-ion and non-lithium-ion batteries [36,44,45]; and for sensing and biosensing [46–48]. In these applications, the conductivity of $Ti_3C_2T_x$ is crucial for ensuring good performance of devices, and it is dependent on the fabrication process used. Due to its metallic nature, $Ti_3C_2T_x$ behavior may be affected by temperature changes significantly; only a few works have investigated the effects of temperature on $Ti_3C_2T_x$ conductivity. For example, in [49] flexible temperature sensors consisting of $Ti_3C_2T_x$ flakes incorporated into polydimethylsiloxane (PDMS) substrates were proposed and characterized. The sensitivity of the device to temperatures ranging from 25 °C to 70 °C is affected by both the response in conductivity of $Ti_3C_2T_x$ and the large coefficient of thermal expansion of PDMS. In [40], the chemical stability of $Ti_3C_2T_x$/Al composites were investigated in the range of 500–700 °C. IJP is one of the printing technologies already used to fabricate MXene-based electrodes [50,51], but, due to the narrow range of the ink viscosity, the MXene content should be kept low and tens of layers of ink should be deposited to obtain low resistance. AJP could reduce the number of deposited layers and the line width, increasing the resolution of the printed pattern. Furthermore, AJP could be an effective fabrication method for electronic components on 3D surfaces or for 3D printing applications. Since AJP is a very recent technology, only a few works have adopted AJP to deposit MXenes. Moreover, the quality of the printed lines should be evaluated to optimize the printing process [52].

In this work, we propose AJP technology to deposit $Ti_3C_2T_x$ ink on PET-based substrates. We studied the geometrical aspect of printed lines and complex patterns (width and thickness of the printed lines), and the printing conditions (different printing parameters and different numbers of printed layers). The measurement of the profiles of the printed lines allows us to estimate both the variability of the process and the resistance of the printed $Ti_3C_2T_x$ lines. Finally, we evaluated the resistance change of $Ti_3C_2T_x$ against temperature in the range − 10– 60 °C and in the range 20–120 °C. We tested the behavior of the ink under different temperature conditions for $Ti_3C_2T_x$ deposited on PET-based film and alumina, as well as the influence of the coating layer on the resistance under different temperature conditions.

2. Materials and methods

2.1. Materials

$Ti_3C_2T_X$ aqueous ink with concentration 40 mg mL^{-1} was prepared according to the procedure described in Section 2.2. $Ti_3C_2T_X$ ink was printed on Novele IJ-220, produced by Novacentrix. IJ-220 is a PET-based substrate with a microporous receptive coating that promotes uniform deposition of many electrically conductive inks. IJ-220 is transparent, with a thickness of 140 µm. Aluminum oxide (Al_2O_3) sheets (50 mm × 50 mm × 0.5 mm) were selected as substrates for studying the temperature effects on the printed lines due to its high melting point (2000 °C) and low coefficient of linear thermal expansion (CTE) (7 10^{-6} K^{-1}). CircuitWorks conductive epoxy CW2400, a two-part silver epoxy with volume resistivity lower than 1 mΩ cm^{-1}, was used to make electrical contact between the printed pads and copper wires (AWG 28). A fast-drying clear spray coating (Printed Clear Lacquer RS 569–290, RS Components) designed for protecting printed circuit boards was used to protect the printed sample in the thermal tests. A single component silicone rubber (SG-250, HBM), which cures at room temperature, was used as an alternative coating. The silicone-based coating is a silicone transparent rubber used primarily to protect printed strain gauges from humidity, mechanical influence, and water.

2.2. Preparation of Ti3C2Tx

In a vented PTFE vessel, 9 M HCl (20 mL, Sigma) was added, followed by the addition of LiF powder (1.6 g, Sigma). The vessel was then placed in a mineral oil bath at 35 °C, stirring at 400 rpm using a magnetic PTFE stirrer bar for 10 min to fully dissolve the LiF and allow the temperature to stabilize. Ti_3AlC_2 MAX phase powder (1 g, Carbon-Ukraine ltd.) was then added in small additions to the vessel over a period of 30 min to avoid overheating of the solution. The solution was then left stirring at 400 rpm at 35 °C for 24 h to obtain etched, multilayer $Ti_3C_2T_x$ MXene. The contents of the vessel were transferred into a pair of 50 mL centrifuge tubes and diluted to a total of 80 mL with deionized water. The dispersion was then sedimented via centrifugation at 5000 rpm using a Thermo Scientific Heraeus Multifuge X1 for 5 min, discarding the supernatant and repeating several times, until the pH of the supernatant had reached at least 6. To delaminate the washed multilayer MXene, the tube was sealed tightly and shaken vigorously by hand and vortex mixing for 30 min. The dispersion was then centrifuged at 1500 rpm for 30 min to sediment any multi-layer MXene or unreacted MAX phase. The supernatant containing delaminated MXene flakes was then

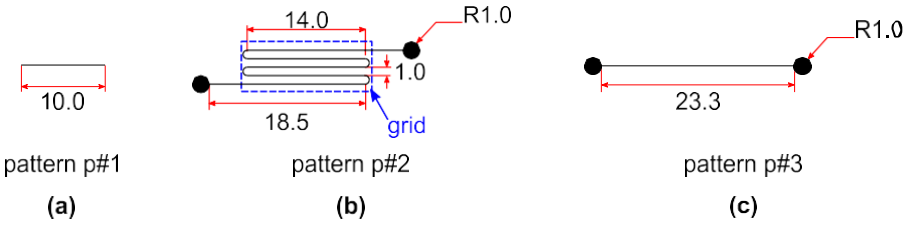

Fig. 1. Patterns used for the validation of the proposed fabrication process for $Ti_3C_2T_x$ deposition: (a) line pattern (p #1); (b) serpentine pattern (p #2); (c) line pattern with pads (p #3). The length of the lines, the radius of the pads (R), and the distance between the lines of p #2 are defined in millimeters. The width of the lines depends on printing parameters.

collected. This supernatant was concentrated via centrifugation at 5000 rpm for 1 h. The sediments were redispersed in a minimum amount of deionized water to obtain the final MXene ink. To determine the concentration of the MXene ink, 100 µl was transferred to a small glass vial and diluted with a 1:1 (v/v) ratio of deionized water and absolute ethanol (Fisher) before being filtered using a pre-weighed 0.25 µm pore nitrocellulose filter membrane (Millipore VSWP) and vacuum filtration flask. The vial and sides of the funnel were washed down with additional 1:1 deionized water and absolute ethanol. Once the filtration was complete, the membrane and MXene filtride were dried overnight in a vacuum desiccator and then weighed to obtain the concentration.

2.3. Design of the printed patterns

The aim of this work was the study of the electrical properties of the $Ti_3C_2T_X$ ink deposited with AJP, a printing technology rarely used for depositing MXene inks. Three different patterns (Fig. 1) were printed on IJ-220 sheets to evaluate the fabrication process and to study the properties of the printed $Ti_3C_2T_X$ ink. Pattern p#1 was used for a full electrical and morphological characterization. Pattern p#2 was printed to evaluate the variability of the process in more complex patterns, while pattern p#3 was used to study the influence of the temperature on the resistance of the printed samples.

2.4. Printing Process and device fabrication

An Optomec AJ-300 aerosol jet printer was used to deposit the $Ti_3C_2T_X$ ink in a controlled manner. The printer, shown in Fig. 2, was configured with a pneumatic atomizer, suitable for inks with a viscosity higher than 10 cP. The Ti3C2Tx aqueous ink was diluted with distilled water by a factor of 1.5 (≃27 mg mL^{-1}). The viscosity of the diluted ink resulted 650 mPa s. Rotational viscosity measurements were performed using a Viscotech VR 3000 MYR Viscometer, model V2L, equipped with a module to test low quantities of ink. 16 mL of the diluted ink was put in the atomizer of the aerosol jet printing system. The bubbler was filled with distilled water. The substrate was placed onto the vacuum plate of the printer, which was heated to 60 °C to promote the drying of the ink during the deposition of multiple overlaid layers of ink. The distance between the vacuum plate and the nozzle tip (of 750 µm diameter) was fixed at 4 mm.

The patterns proposed in Section 2.3 were designed in AutoCAD software, which provided an output file compatible with the process control software of the printer. We selected two combinations of printing parameters (Table 1) because we wanted to obtain printed tracks with different widths and thicknesses for testing the fabrication process under different printing conditions. According to the application, the pattern was printed several times to increase the thickness of the deposited ink, by overlaying several printed layers (N_{layers}).

After printing the pattern, the printed samples were dried at 60 °C for 30 min in an oven to promote solvent evaporation. For thermal characterization of the printed ink, we glued copper wires on the circular pads with conductive epoxy. The epoxy was cured at 60 °C for 10 min, as recommended by the manufacturer.

For tests requiring a protective layer for the printed samples, we used a spray coating or deposited silicone rubber onto the printed sample. According to the manufactures' recommendations, the curing of the coating layers took place at room temperature (RH > 30%) for 24 h.

2.5. Experimental procedure for the characterization

A diamond stylus-based profilometer was used for step height measurements (Alpha-Step IQ Kla Tencor), operating with an accuracy of 0.1%. The stylus was moved in the direction of the linewidth (x-axis), and the thickness was measured by taking the movement of the stylus along the z-axis. The acquired x-z curves were adjusted in order to locate the points corresponding to the substrate around the z-axis. The cross-sectional area of the lines was determined by calculating the area between the plotted curve and z = 0 utilizing a Riemann sum-type approach. The deposition of the ink by AJP was evaluated by acquiring the profile of three cross sections of the sample, one in the middle and two 2 mm from the end of the line (or of the grid in the case of serpentine pattern).

An optical microscope with trinocular zoom 0.8x–5x–LED, equipped with a devoted HDMI MDH5 camera, was used to acquire the images (NB50T, Orma Scientific).

The current signal was acquired using a source meter with an accuracy lower than 0.2% (Palmsense 3).

The resistance of the printed sample was measured using a multimeter (HP 34401 A, Agilent Scientific Instruments I). A vacuum oven (Vacutherm™ VT 6130 P, Thermo Scientific™) and a climatic chamber (UC 150/70, Perani) were used for thermal characterization in the range 20–120 °C and − 10–65 °C, respectively. The experimental setup is outlined in Fig. 3. A custom-made LabVIEW application (VI) was developed to control the temperature and to synchronize the acquisition of multiple HP 34401 A multimeters. A class A Pt100 sensor was placed near the samples under testing and was used as the reference temperature sensor to measure the temperature near the samples. The resistance readings were acquired by the VI at 1 S/s for each multimeter.

3. Results and discussion

3.1. Morphology of printed $Ti_3C_2T_X$-based lines

The p #1 pattern (Fig. 1a) was printed to evaluate the deposition of $Ti_3C_2T_x$ ink by measuring the profile of the printed lines and their electrical resistance. On a portion of IJ-220 film, we printed a row of six 10 mm-long lines (pattern p #1) with a different number of overlaid printed layers (N_{layers}). We kept fixed the printing parameters to the values of SET #1 (Table 1), and this allowed us to define the line width. We selected N_{layers} = 1, 2, 3, 4, 5, and 10 in

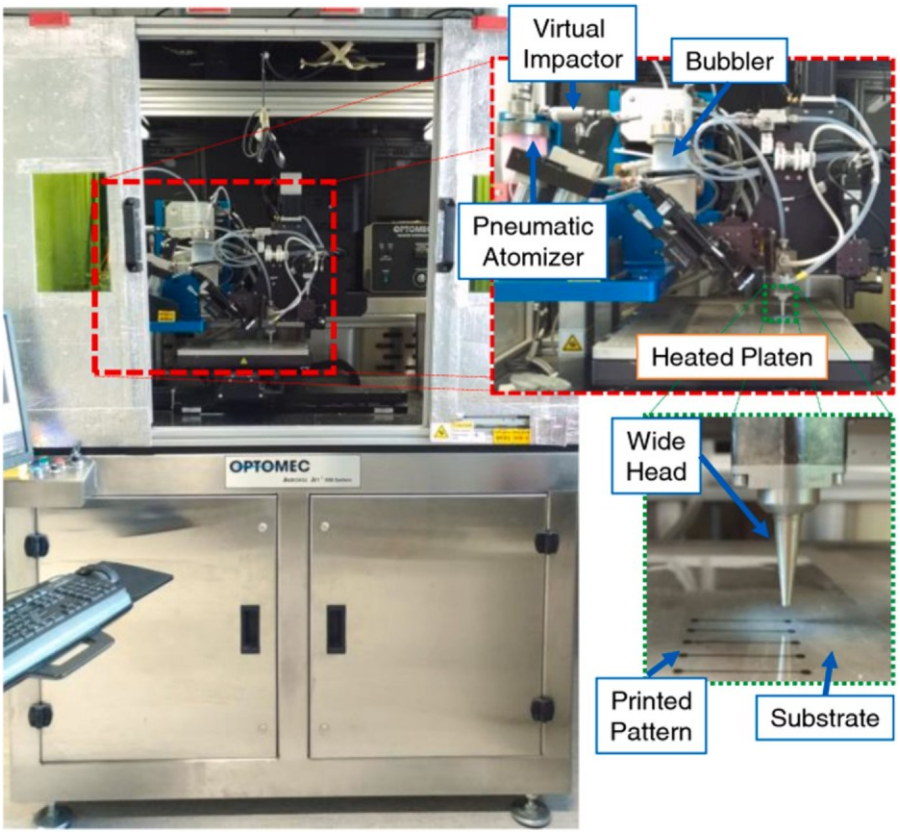

Fig. 2. Aerosol jet printing system for printing $Ti_3C_2T_x$ ink (Optomec AJ 300). The inset on the top highlights the main components of the printing system; the inset on the bottom shows the printed lines during the printing process.

Table 1
Printing process parameters for different patterns and.

Parameter		SET #1	SET #2
Sheath gas flow	SCCM	1000	800
Atomizer gas flow	SCCM	650	1400
Exhaust gas flow	SCCM	500	1300
Printing speed	mm/s	2	1

order to find the relationship between N_{layers} and the thickness of the lines. The distance between two lines was 5 mm.

The ink deposition was evaluated by measuring the profile of the printed lines at 2 mm from both its ends (E1 and E2) and in the middle (M) of the line. The three measured profiles are grouped in the same plot (Fig. 4a–f). As expected, the cross-section area of the line increases as a function of the number of layers. Considering the acquired profiles of the same line, the overall deposition of the ink can be considered uniform along the line and the thickness is defined as the maximum height located in the central portion of the profile. The mean width

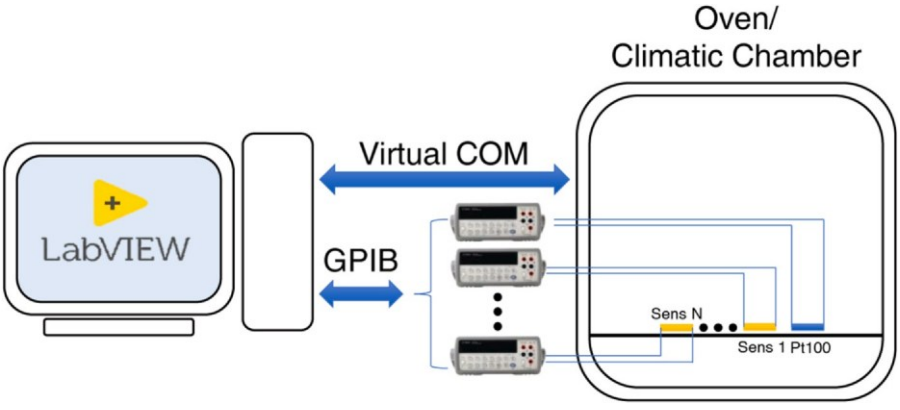

Fig. 3. Block diagram of the experimental setup used for the thermal characterization of printed $Ti_3C_2T_x$ samples. A custom virtual instrument (VI) developed in the LabVIEW environment controls the temperature setpoint of the chamber and the multimeters for the resistance acquisition. The VI cyclically changes the temperature setpoint of the chamber according to the experiment protocol, while the Pt100 is used as the reference sensor to measure the temperature near the printed samples. The resistance of the Pt100 is acquired by a multimeter and it is converted into a temperature measurement, while the other multimeters acquire the resistance of the printed samples (with a sample rate of 1 S/s).

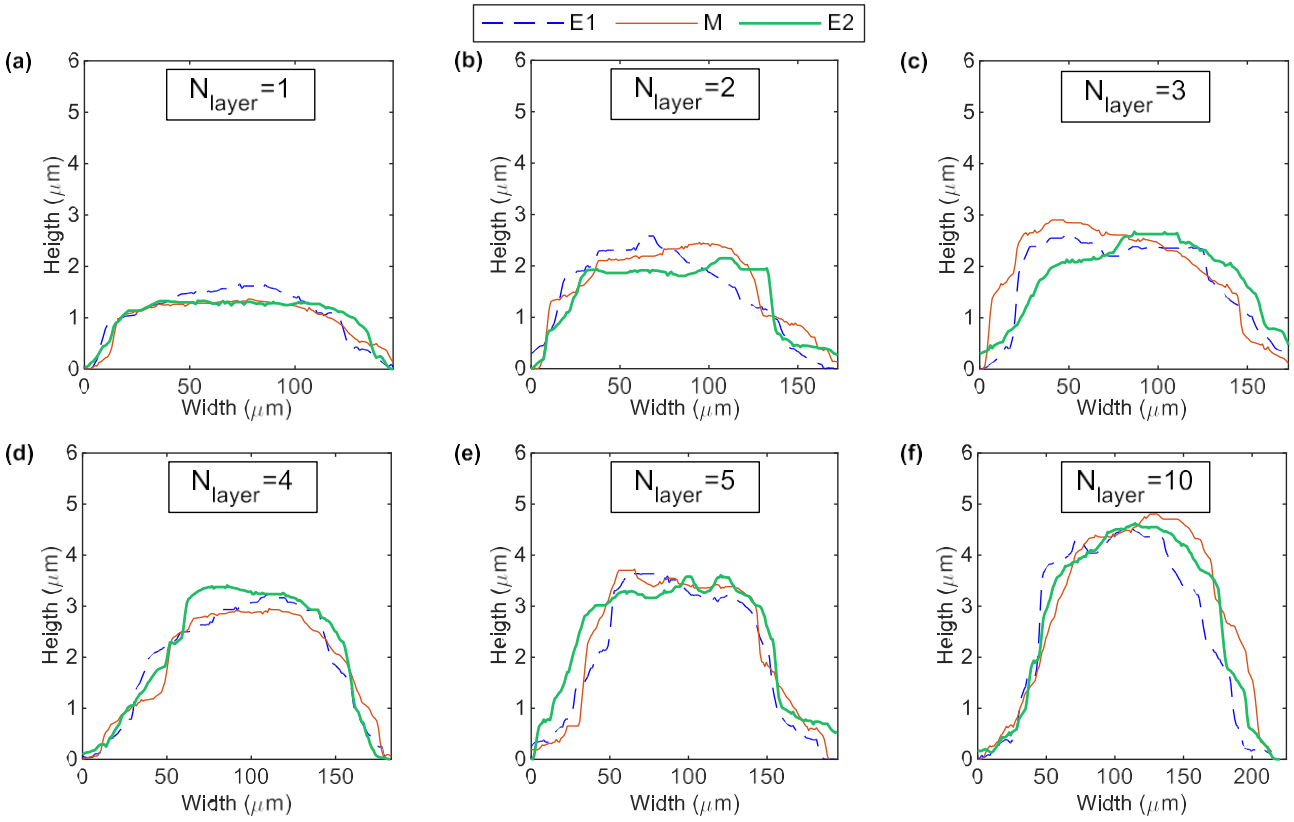

Fig. 4. Profile of six printed $Ti_3C_2T_x$ lines (pattern p #1) as a function of the number of overlaid printed layers, from 1 to 5 ((a)–(e)) and 10 (f). The profiles were measured with an optical profilometer in three points of the printed lines: at 2 mm from the ends (E1 and E2) and in the middle (M).

calculated for the three acquired profiles of the same line is depicted in Fig. 5a as a function of N_{layers}. The error bars represent the minimum and maximum values of the measured widths. The mean width is (150 ± 2) μm for the line with N_{layers} = 1 and it increases to (216 ± 3) μm for the line with N_{layers} = 10. The width measured on each profile deviates from its mean value by less than 1.3%, and this result is consistent with the position repeatability (2 μm) and position accuracy (5 μm) declared by the printer manufacturer. The relationship between N_{layers} and the linewidth is not linear, but it can be approximated with a second-order polynomial curve by using the least-squares method (adjusted R-squared = 0.9696). Similar results were obtained for the cross-sectional area of the lines (Fig. 5b) and for the maximum height of the profiles (Fig. 5c). The area-N_{layers} curve and thickness-N_{layers} curve are well fitted with second-order polynomial curves, (R-squared equal to 0.9925 for area-N_{layers} regression curve and 0.9898 for the thickness-N_{layers} regression curve). The cross-sectional area deviates from its mean value by less than 6%, while the maximum deviation for the thickness is less than 10%, though this decreases to 2.6% for N_{layers} > 3. Excluding the case of N_{layers} equal to 10, the area-N_{layers} curve and thickness-N_{layers} curve could be well fitted by a linear regression (adjusted R-squared > 0.97). By increasing the number of layers, the edges get smoother, especially when N_{layers} = 10, and this can justify the increase in line width.

3.2. *Resistance of printed $Ti_3C_2T_X$ lines*

We used the same printing procedure to print a 6 × 6 array of 36 lines (pattern p #1). The lines in the same column have the same N_{layers}. As for

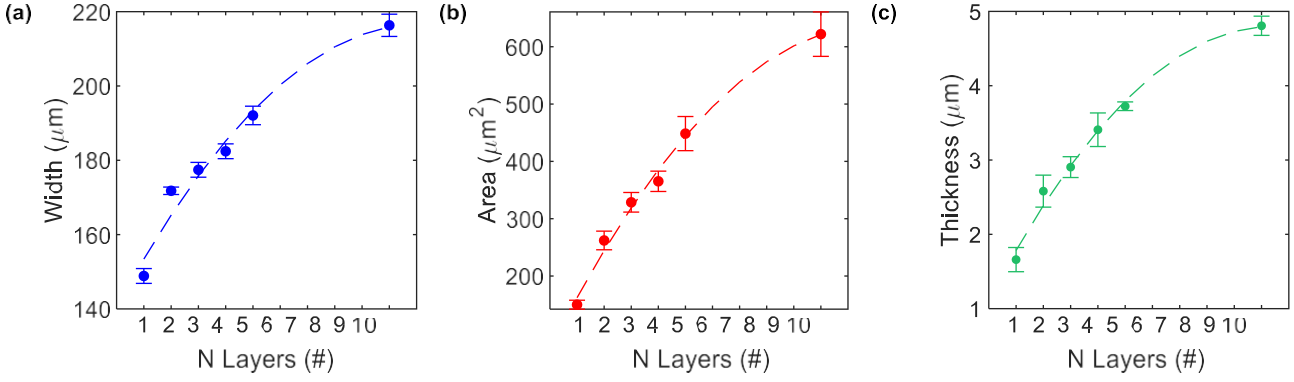

Fig. 5. (a) Mean width, (b) mean area of the section, and (c) mean maximum height of six printed $Ti_3C_2T_x$ lines (pattern p #1) as a function of the number of printed layers, from 1 to 5 and 10. These mean values were calculated considering the three acquired profiles E1, E2, and M shown in Fig. 4, while the bars include the three values obtained from the acquired profiles E1, E2, and M. The dashed lines are the second-order polynomial curves obtained by using the least-squares method and provide the best fit of the data.

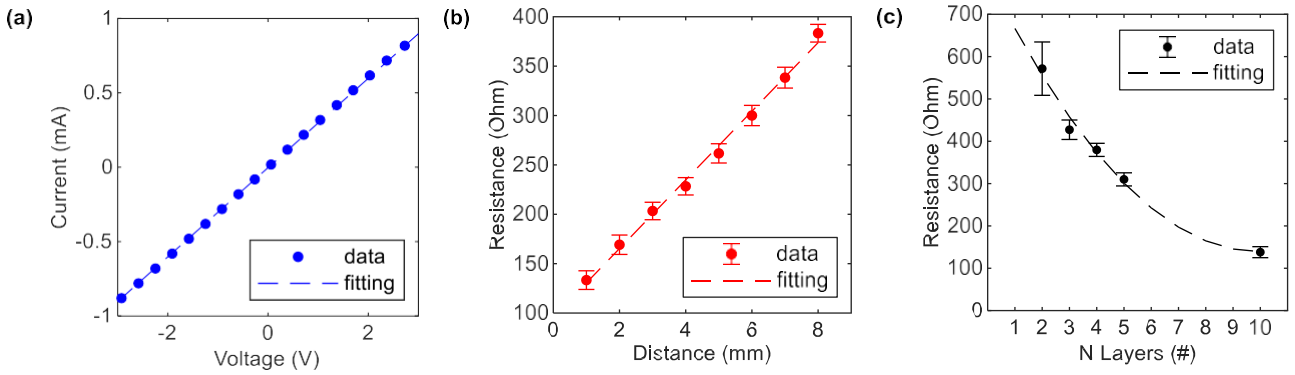

Fig. 6. (a) Voltage-Current characteristic of a printed line (pattern p #1) with five printed layers by using the four-point probe method; the distance between the voltage probes is 6 mm. (b) Resistance of a printed line (pattern p #1) with five printed layers in the function of the distance between the two probes. (c) Resistance of six identical printed lines (pattern p #1) as a function of the number of printed layers. The bar includes the resistance measured on six identical lines with five printed layers when the distance of probes is 6 mm.

the previous case, N_{layers} was varied from 1 to 10. We investigated the electrical properties of the printed $Ti_3C_2T_x$ ink. The voltage-current (V-I) curve of a printed line (N_{layers} = 5) is shown in Fig. 6a, as a representative example. As expected, the relationship between the measured current and the voltage is linear, with negligible y-intercept (R-squared = 0.9997). The standard deviation was considered equal to the accuracy of the instrumentation (0.2% of the reading) and thus it was not shown in the figure due to its low value. This representative line shows a resistivity of 23 μΩ m. Similar results were obtained for the other lines with different N_{layers}. V–I results confirm that the printed $Ti_3C_2T_x$ tracks can be considered to be resistive, also regardless of the N_{layers} value. For this reason, the resistance of the printed tracks was measured by a high-performance multimeter (HP34401A). The quality of the printing process was also confirmed by changing the distance between the two probes from 1 mm to 8 mm. The relationship between the distance of the probes and the measured resistance of a line with N_{layers} = 5 is depicted in Fig. 6b. The error bars are the standard deviation calculated on 6 measurements taken on the same sample. The positioning accuracy was estimated to be 200 μm. Also in this case, the curve is well fitted by a linear regression by using the least-square method (R-squared = 0.9951). Fig. 6c shows the measured resistance of the printed lines as a function of N_{layers}. The resistance was measured when the distance between the probe was 6 mm. The dots in the plot represent the mean value, and the error bars include the minimum and the maximum resistance values measured on the 6 identical lines. The resistance of the lines with N_{layers} = 1 is not shown in the figure since we measured a resistance outside the instrument range. The data can be fitted by a second-order polynomial curve (adjusted R-squared = 0.9871). This trend is similar to the results obtained for the width, the cross-sectional area, and the thickness as a function of N_{layers}.

Combining the geometrical results (mean width $\bar{w}$ and line length $\bar{l}$) and the measured resistance ($\underline{R}$) shown in Fig. **5**6, we calculated the mean sheet resistance $\bar{R}_s$ as a function of N_{layers} higher than one by using Eq. (3.1).

$$\bar{R}_s = R\frac{\bar{w}}{\bar{l}} \tag{3.1}$$

$\bar{R}_s$ decreases from 16 Ω/sq (N_{layers} = 2) to 5 Ω/sq (N_{layers} = 10). This finding demonstrate the possibility to print conductive lines or resistors by changing the number of layers, as already proved in [51] by using the inkjet printing technology.

3.3. Morphology and electrical conductivity of printed $Ti_3C_2T_x$ sample with more complex geometry

We printed pattern p #2 in order to validate the fabrication process for more complex patterns and longer printed tracks. The serpentine pattern is commonly used to fabricate piezoresistive or temperature sensors. The mean length of the serpentine pattern is 85 mm, the radius of the pads is 1 mm. We assigned the values of the SET #2 listed in Table 1 to the printing parameters and we repeated the printing process five times (N_{layers} = 5). The final printed sample is shown in Fig. 7. Due to the different values of the printing parameters, the width of the tracks changes with respect to the printed lines of Sections 3.1 and 3.2. This result is confirmed also by the profile measurements, which allow us to calculate the width and the spacing between the parallel lines. The profile was measured in three points of the grid. The profile of the section in the middle of the grid is shown in Fig. 8, as a representative example. Considering the three profiles (each one includes five cross sections) and determining the width of each line for a total of 15 line cross sections, the mean width (w) was determined to be (365 ± 15) μm, with a maximum height of (9.25 ± 0.6) μm. The distance between two parallel lines (d) was determined to be (998 ± 29) μm. The results confirm that the deposition and curing of the ink is uniform during the printing of the pattern; for example, the standard deviation for the line width is 15 μm (4% of the mean value) and the resistance for the six identical printed serpentine patterns (pattern p #2) deviates of 4% from the mean value. The resistivity is comparable with the one obtained for printed lines.

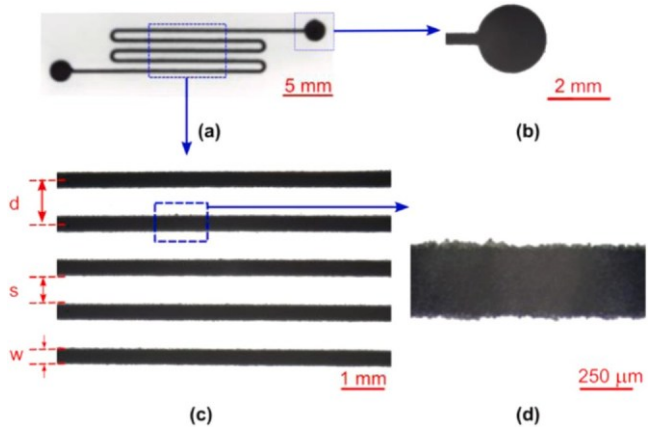

Fig. 7. (a) Optical image of a representative printed with pattern p #2, fabricated on IJ-220 sheet. Enlarged view (b) of the right pad, (c) of the printed grid, and (c) of one parallel line of the grid. The distance (d) between two consecutive lines of the grid is defined in the pattern design. The width (w) of the lines and the resulting spacing s (the difference between d and w) were affected by the printing parameters (Table 1, SET #2) and they were measured by the profilometer.

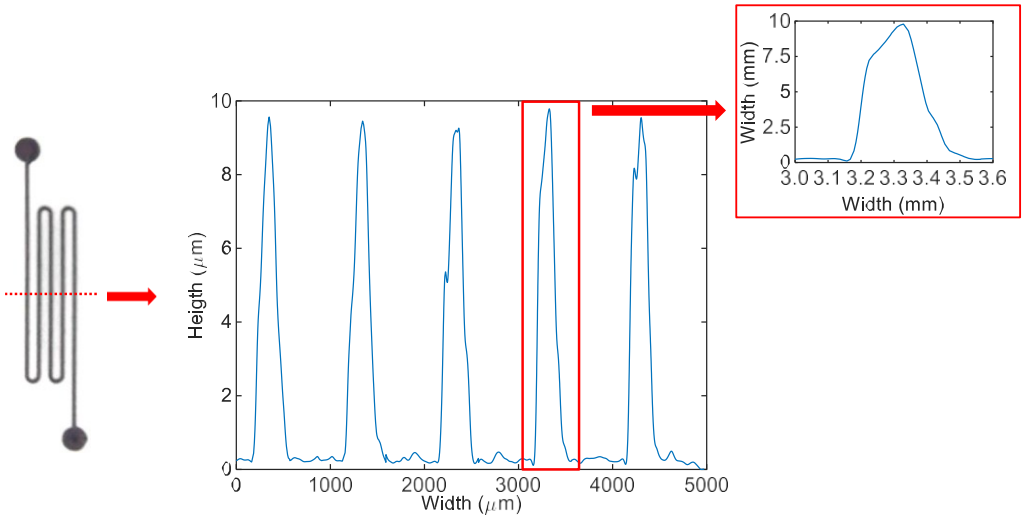

Fig. 8. Profile of the printed sample (on the left) measured in the middle of the grid, as indicated by the dashed line drawn on the picture of the sample. An enlarged view of the profile of the fourth printed line is shown in the inset on the right.

3.4. Influence of the temperature on $Ti_3C_2T_X$ resistance

Finally, we printed pattern p #3 to define the influence of the temperature on the $Ti_3C_2T_x$ resistance. We assigned the same values of the previous test (SET #2 of Table 1) to the printing parameters and N_{layers} = 10. We obtained similar results (profile and visual inspection using optical microscopy) to those obtained on the printed serpentine patterns (Section 3.3).

For continuous monitoring, we glued copper wires on the circular pads with silver conductive epoxy.

In the first test, the printed line and a Pt100 sensor were put inside a temperature-controlled oven. The temperature setpoint was automatically changed every 20 min with a step of 10 °C, in the range of 20–120 °C during the heating phase. The duration of each temperature step ensured the stabilization of the oven temperature (error band < 0.1% of the setpoint over the last five minutes). During the cooling phase, the oven was turned off to induce an uncontrolled temperature decrease. The temperature measured by the Pt100 is shown in Fig. 9a. Measuring the resistance R of the Pt100 with a multimeter, the temperature T was calculated through Eq. (3.2), according to the sensor datasheet.

$$T = \frac{(R\_100)}{0.00385} \tag{3.2}$$

Fig. 9b shows the relative changes of resistance normalized to the resistance at 20 °C ($\Delta R/R_{20}$) of a representative $Ti_3C_2T_x$ line during heating and cooling phases as a function of the temperature T. For comparison, $\Delta R/R_{20}$ of Pt100 sensor is also shown. The data points are the mean value of 500 measurements (corresponding to the last five minutes) before changing the temperature setpoint. The resistance change in this period was lower than 0.1% of the mean value. According to these results, the temperature affects $Ti_3C_2T_x$ resistance; for example, in the heating phase, the $Ti_3C_2T_x$ resistance changes of 20% in the range 20-120 °C, although the resistance increase is higher in Pt100 sensor (35% in the same range). Despite the $\Delta R/R_{20}$-T characteristics being non-linear, $\Delta R/R_{20}$-T could be well

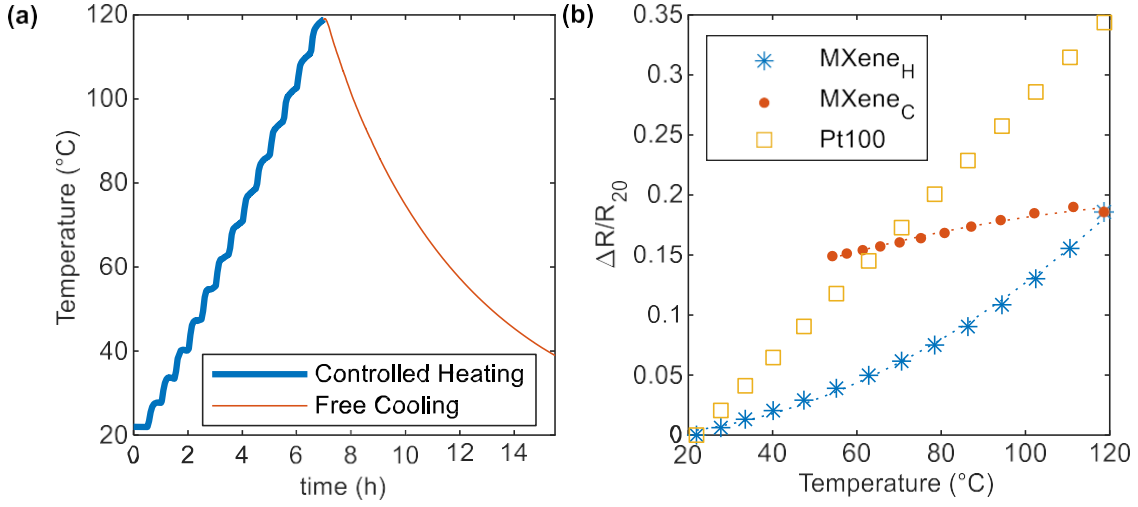

Fig. 9. Resistance change of printed $Ti_3C_2T_x$ as a function of the temperature. (a) The temperature was measured by a Pt100 inside the chamber. The temperature during heating is controlled every 30 min by changing the temperature setpoint, while during the cooling phase the heater was turn off, without controlling the temperature. (b) $Ti_3C_2T_x$ response over temperature change during heating phase (line with asterisk markers) and cooling phase (line with dot markers), compared to Pt100 response (line with square markers). The output of both sensors is normalized on their value at 20 °C, at the beginning of the test. The dotted lines represent the approximation of the curve with a second-order polynomial curve.

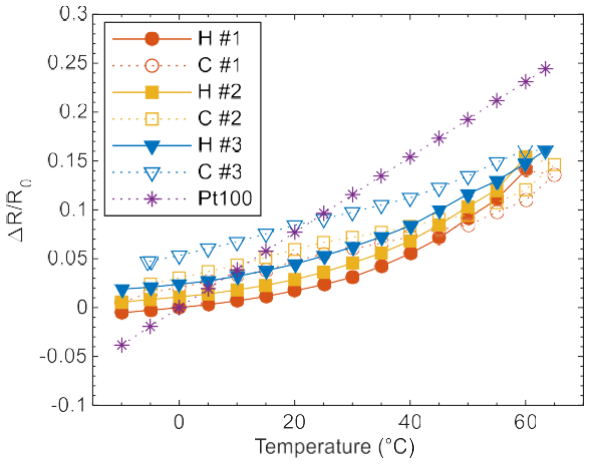

Fig. 10. Influence of the temperature on the resistance of printed $Ti_3C_2T_x$ (pattern p #3) on Al_3O_2 substrate during three thermal cycles, starting with the heating phase (H) followed by the cooling phase (C). The printed ink is protected by a conformal coating. The resistance change is normalized on the resistance value measured at 20 °C in the H phase of the first cycle. The humidity inside the climatic chamber remained under 30%. The line with asterisk markers represents the resistance response of the Pt100 sensor.

fitted with a second-order polynomial curve (adjusted R-squared = 0.9975), and this result could be used to compensate for temperature effects on $Ti_3C_2T_x$ resistance in performance-critical applications. In the cooling phase, the resistance change is lower. The uncontrolled cooling could explain this behavior; indeed, during the cooling phase, the temperature changes continuously, while during the heating phase the temperature setpoint was controlled and kept fixed. Secondly, the shrinking of the PET substrate during cooling may be different from its expansion during the heating phase, and this affects the printed $Ti_3C_2T_x$ response to temperature. Despite that PET can withstand temperatures over 150 °C, its glass transition temperature is around 70 °C. Finally, it is well known that the $Ti_3C_2T_x$ oxidizes in air, possibly affecting its final resistance [53].

For this reason, the same pattern was printed on an Al_2O_3 substrate. The CTE of Al_2O_3 is significantly lower than the PET CTE (7 10^{-5} K^{-1}), and thus reduces the piezoresistive effects of the ink due to thermal expansion of the substrate. Furthermore, it is more stable in the selected temperature range. In the first test, a spray coating was deposited over a $Ti_3C_2T_x$ line printed on Al_2O_3 substrate to protect the ink from the humidity and to minimize the oxidation due to the air. Due to its properties, the coating layer was expected to reduce the sensitivity of the printed $Ti_3C_2T_x$ ink. Wires were glued before the coating. The final device was put inside the climatic chamber. The temperature chamber was increased from − 10 °C and 60 °C in the heating phase (H) and then was decreased in the same temperature range in the cooling phase (C), and this thermal cycle was repeated three times. The relative resistance change as a function of the temperature measured by the Pt100 is shown in Fig. 10. The relative resistance change was normalized on the resistance measured at 0 °C of the first cycle ($R_{0,1}$). According to the previous results, the resistance of the printed line increases with temperature (14.5% of $R_{0,1}$) less than Pt100 (26.9% of $R_{0,1}$) in the range − 10–60 °C. A thermal hysteresis effect was also observed for the printed line; the hysteresis is 28% in the worst case, and it is maximum at 20 °C. The duration of each cycle was approximately four hours, and this could explain the resistance drift between cycles.

The same test was repeated on three samples: 1) a printed line on Al_2O_3 substrate with the fast-drying clear coating, 2) a printed line on Al_2O_3 substrate with silicone-based coating and 3) a printed line on PET with silicone-based coating. The results are shown in Fig. 11. In this case, the relative resistance change in one cycle was normalized to the resistance measured at 0 °C of the same cycle. This allows us to focus on the thermal effect on the resistance, minimizing the effect of resistance drift over time. The response of the $Ti_3C_2T_x$ lines to temperature changes depends both on the coating layer and on the substrate: it is maximized for printed lines on Al_2O_3 with spray coating and minimized for printed lines on PET. The thickness of the spray coating (some tens of microns) is lower than that of the rubber coating (hundreds of microns) and this affects insulation against temperature fluctuation. Furthermore, the silicone coating is typically used to reduce the oxidation of the sensitive layer and thus the resistance increase over time. The higher thermal

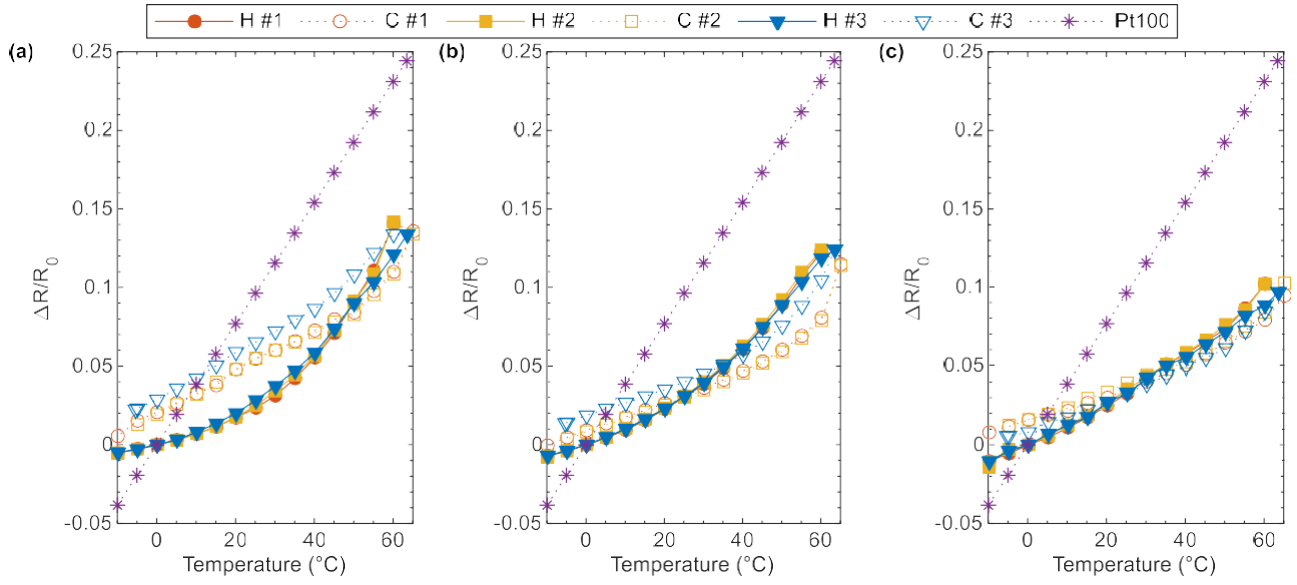

Fig. 11. Influence of the temperature on the resistance of printed $Ti_3C_2T_x$ (pattern p #3) (a) on Al_3O_2 substrate and protected by an acrylic copolymer (b) on Al_3O_2 substrate and protected by a silicone-based coating (c) on PET-based substrate and protected by a silicone-based coating. The printed samples were placed in the climatic chamber at the same moment and they were monitored during three thermal cycles, starting with the heating phase (H) followed by the cooling phase (C). The resistance changes in one cycle are normalized on the resistance values measured at 20 °C in the H phase of the same cycle. The humidity inside the climatic chamber remained under 30%. The line with asterisk markers represents the resistance response of the Pt100 sensor.

conductivity of Al_2O_3 (23 W m^{-1} K^{-1}) with respect to the one of PET (0.15–0.4 W m^{-1} K^{-1}) contributes more to the thermal effects on the $Ti_3C_2T_x$. The normalization of the cyclic curves on the resistance value at 0 °C of the same cycle allows us to conclude that the resistance change over the temperature of each printed line could be fitted with the same approximation curve, especially in the heating phase. Also in this case, a second-order polynomial curve can fit well the data (adjusted R-square > 0.996).

The results show that $Ti_3C_2T_X$ has a lower sensitivity to the temperature than metallic nanoparticle inks in a range lower than 70 °C (the behavior of metallic ink is similar to Pt100 behavior as confirmed in [28]), and thus $Ti_3C_2T_X$ could be preferred for applications with variable operating temperature sensors. Otherwise, sensors based on $Ti_3C_2T_X$ could be preferred for applications that require biocompatibility [54] or a low-temperature process. These results on the effects of the temperature on the $Ti_3C_2T_X$ printed lines could be used to compensate for thermal influence on the electrical behavior of $Ti_3C_2T_X$-based devices.

4. Conclusions

In this work, a printing method based on aerosol jet printing was proposed to selectively deposit $Ti_3C_2T_X$ ink on PET-based sheets. Lines and serpentine patterns were printed and studied, measuring the surface cross section and the electrical properties of the printed structures. We measured the profile of printed lines in the width direction, and we found that the cross-sectional area deviates from its mean value by less than 6%. By changing the number of overlaid printed layers (N_{layers}), the thickness increases from 1.6 µm to 4.8 µm, and the width from 150 µm to 216 µm for N_{layers} between 1 and 10. Compared to the results of [51], the thickness of the lines fabricated using AJP with N_{layers} = 10 was 50 times higher, with a lower width, as expected. The relationship between the geometrical changes and N_{layers} can be modeled with a second-order polynomial curve. The conductivity of $Ti_3C_2T_X$ lines is obtained for N_{layers} = 2 at least, and the resistance decreases with increasing values of N_{layers}. The resistivity resulted 23 µΩ·m. The ink deposition is uniform along the length, also in the case of longer printed lines and of serpentine patterns; indeed, the resistance increases linearly with the distance between the two measurement points. In this work, the temperature effects on the resistance of pure $Ti_3C_2T_X$ structures were investigated for the first time. In the range from 20 °C to 120 °C, the resistance increases by 18%, while the resistance of $Ti_3C_2T_X$ printed on alumina increases by 15% in the range − 10–60 °C. When the printed layer is protected by a coating layer (acrylic or silicone), the sensitivity of $Ti_3C_2T_X$ slightly is reduced under continuous heating "ramp" conditions, and the oxidation of the ink was inhibited. The presented analysis indicates that the adopted fabrication process based on AJP enables the fabrication of $Ti_3C_2T_X$ structures with small variability and stable electrical characteristics. Furthermore, in comparison with other metal inks (silver, platinum, etc.), the resistance change of $Ti_3C_2T_X$ with temperature is smaller. Additionally, $Ti_3C_2T_X$ is a promising material for applications with biocompatibility requirements. All these features are essential for the development of aerosol jet printed sensors (electrochemical, piezoresistive, and gas sensors) and electrodes for energy storage applications on plastic foils and 3D surfaces.

CRediT authorship contribution statement

Michela Borghetti: Conceptualization, Methodology, Software, Validation, Formal analysis, Investigation, Data curation, Writing – original draft, Writing – review & editing, Visualization, Project administration. **Mauro Serpelloni:** Conceptualization, Methodology, Writing – review & editing. **Emilio Sardini:** Conceptualization, Resources, Writing – review & editing, Supervision, Funding acquisition. **Dahnan Spurling:** Validation, Investigation, Writing – review & editing. **Valeria Nicolosi:** Methodology, Resources, Writing – review & editing, Funding acquisition.

Declaration of Competing Interest

The authors declare that they have no known competing financial interests or personal relationships that could have appeared to influence the work reported in this paper.

References

[1] J. Chang, X. Zhang, T. Ge, J. Zhou, Fully printed electronics on flexible substrates: high gain amplifiers and DAC, Org. Electron. 15 (2014) 701–710, https://doi.org/10.1016/j.orgel.2013.12.027

[2] M.U. Khan, G. Hassan, M. Awais, J. Bae, All printed full range humidity sensor based on Fe2O3, Sens. Actuators A Phys. 311 (2020) 112072, https://doi.org/10.1016/j.sna.2020.112072

[3] S. Khan, S. Ali, A. Khan, M. Ahmed, B. Wang, A. Bermak, Inkjet printing of multi-stripes based deflection monitoring sensor on flexible substrate, Sens. Actuators A Phys. 323 (2021) 112638, https://doi.org/10.1016/j.sna.2021.112638

[4] D. Sinar, G.K. Knopf, Disposable piezoelectric vibration sensors with PDMS/ZnO transducers on printed graphene-cellulose electrodes, Sens. Actuators A Phys. 302 (2020) 111800, https://doi.org/10.1016/j.sna.2019.111800

[5] P. Andersson Ersman, R. Lassnig, J. Strandberg, D. Tu, V. Keshmiri, R. Forchheimer, S. Fabiano, G. Gustafsson, M. Berggren, All-printed large-scale integrated circuits based on organic electrochemical transistors, Nat. Commun. 10 (2019) 1–9, https://doi.org/10.1038/s41467-019-13079-4

[6] Z. Gozutok, O. Agırbas, M.I. Bahtiyari, A.T. Ozdemir, Low-voltage textile-based wearable heater systems fabricated by printing reactive silver inks, Sens. Actuators A Phys. 322 (2021) 112610, https://doi.org/10.1016/j.sna.2021.112610

[7] S. Akbari, A.H. Sakhaei, S. Panjwani, K. Kowsari, Q. Ge, Shape memory alloy based 3D printed composite actuators with variable stiffness and large reversible deformation, Sens. Actuators A Phys. 321 (2021) 112598, https://doi.org/10.1016/j.sna.2021.112598

[8] A. Dutta, R. Nayak, M. Selvakumar, D. Devadiga, P. Selvaraj, S.S. Kumar, Graphite/copper nanoparticle-based high-performance micro supercapacitor with porous wet paper-based PVA-PVP blend polymer electrolyte, Mater. Lett. 295 (2021) 129849, https://doi.org/10.1016/j.matlet.2021.129849

[9] J. Xu, X. Hu, X. Wang, X. Wang, Y. Ju, S. Ge, X. Lu, J. Ding, N. Yuan, Y. Gogotsi, Low-temperature pseudocapacitive energy storage in Ti3C2Tx MXene, Energy Storage Mater. 33 (2020) 382–389, https://doi.org/10.1016/j.ensm.2020.08.029

[10] Z. Liu, Z.S. Wu, S. Yang, R. Dong, X. Feng, K. Müllen, Ultraflexible in-plane micro-supercapacitors by direct printing of solution-processable electrochemically exfoliated graphene, Adv. Mater. 28 (2016) 2217–2222, https://doi.org/10.1002/adma.201505304

[11] S. Khan, L. Lorenzelli, R.S. Dahiya, Technologies for printing sensors and electronics over large flexible substrates: a review, IEEE Sens. J. 15 (2015) 3164–3185, https://doi.org/10.1109/JSEN.2014.2375203

[12] P. He, J. Cao, H. Ding, C. Liu, J. Neilson, Z. Li, I.A. Kinloch, B. Derby, Screen-printing of a highly conductive graphene ink for flexible printed electronics, ACS Appl. Mater. Interfaces 11 (2019) 32225–32234, https://doi.org/10.1021/acsami.9b04589

[13] V. Beedasy, P.J. Smith, Printed electronics as prepared by inkjet printing, Mater. (Basel) 13 (2020) 1–23, https://doi.org/10.3390/ma13030704

[14] Y.D. Chen, V. Nagarajan, D.W. Rosen, W. Yu, S.Y. Huang, Aerosol jet printing on paper substrate with conductive silver nano material, J. Manuf. Process. 58 (2020) 55–66, https://doi.org/10.1016/j.jmapro.2020.07.064

[15] K.-S. Kwon, M.K. Rahman, T.H. Phung, S. Hoath, S. Jeong, J.S. Kim, Review of digital printing technologies for electronic materials, Flex. Print. Electron. (2020), https://doi.org/10.1088/2058-8585/abc8ca

[16] H. Matsui, Y. Takeda, S. Tokito, Flexible and printed organic transistors: from materials to integrated circuits, Org. Electron. 75 (2019) 105432, https://doi.org/10.1016/j.orgel.2019.105432

[17] A.D. Valentine, T.A. Busbee, J.W. Boley, J.R. Raney, A. Chortos, A. Kotikian, J.D. Berrigan, M.F. Durstock, J.A. Lewis, Hybrid 3D printing of soft electronics, Adv. Mater. 29 (2017) 1–8, https://doi.org/10.1002/adma.201703817

[18] R. Guo, B. Cui, X. Zhao, M. Duan, X. Sun, R. Zhao, L. Sheng, J. Liu, J. Lu, Cu-EGaIn enabled stretchable e-skin for interactive electronics and CT assistant localization, Mater. Horiz. 7 (2020) 1845–1853, https://doi.org/10.1039/c9mh02066g

[19] S. Calvi, F. Maita, M. Rapisarda, G. Fortunato, A. Valletta, V. Preziosi, A. Cassinese, L. Mariucci, Gravure printed organic thin film transistors: Study on the ink printability improvement, Org. Electron. 61 (2018) 104–112, https://doi.org/10.1016/j.orgel.2018.06.026

[20] M. Pietsch, S. Schlisske, M. Held, N. Strobel, A. Wieczorek, G. Hernandez-Sosa, Biodegradable inkjet-printed electrochromic display for sustainable short-life-cycle electronics, J. Mater. Chem. C 8 (2020) 16716–16724, https://doi.org/10.1039/d0tc04627b

[21] H. Zhang, S.K. Moon, T.H. Ngo, 3D printed electronics of non-contact ink writing techniques: status and promise, Int. J. Precis. Eng. Manuf. - Green Technol. 7 (2020) 511–524, https://doi.org/10.1007/s40684-019-00139-9

[22] N.J. Wilkinson, M.A.A. Smith, R.W. Kay, R.A. Harris, A review of aerosol jet printing—a non-traditional hybrid process for micro-manufacturing, Int. J. Adv. Manuf. Technol. 105 (2019) 4599–4619, https://doi.org/10.1007/s00170-019-03438-2
[23] Q. Jing, Y.S. Choi, M. Smith, C. Ou, T. Busolo, S. Kar-Narayan, Freestanding functional structures by aerosol-jet printing for stretchable electronics and sensing applications, Adv. Mater. Technol. 4 (2019) 1900048, https://doi.org/10.1002/admt.201900048
[24] N.X. Williams, N. Watson, D.Y. Joh, A. Chilkoti, A.D. Franklin, Aerosol jet printing of biological inks by ultrasonic delivery, Biofabrication 12 (2020) 025004, https://doi.org/10.1088/1758-5090/ab5cf5
[25] M. Serpelloni, E. Cantù, M. Borghetti, E. Sardini, Printed smart devices on cellulose-based materials by means of aerosol-jet printing and photonic curing, Sensors 20 (2020) 841, https://doi.org/10.3390/s20030841
[26] N.J. Wilkinson, M. Lukic-Mann, M.P. Shuttleworth, R.W. Kay, R.A. Harris, Aerosol jet printing for the manufacture of soft robotic devices, RoboSoft 2019 - 2019 IEEE Int. Conf. Soft Robot (2019) 496–501, https://doi.org/10.1109/ROBOSOFT.2019.8722766
[27] A. Delage, N. Delhote, S. Verdeyme, B. Bonnet, L. Carpentier, C. Schick, T. Chartier, C. Chaput, Aerosol jet printing of millimeter wave transmission lines on 3D ceramic substrates made by additive manufacturing, IEEE MTT-S Int. Microw. Symp. Dig. (2018) 1557–1560, https://doi.org/10.1109/MWSYM.2018.8439498
[28] M. Borghetti, E. Cantù, E. Sardini, M. Serpelloni, Future sensors for smart objects by printing technologies in industry 4.0 scenario, Energies 13 (2020) 5916, https://doi.org/10.3390/en13225916
[29] C. Yi, R. Fedderwitz, D. Park, C. Ding, G.-Q. Lu, J. Fleischer, P. Li, P. Kofinas, S. Das, D.R. Hines, Fully printed resonance-free broadband conical inductors using engineered magnetic inks, Addit. Manuf. 44 (2021) 102034, https://doi.org/10.1016/j.addma.2021.102034
[30] C. Cooper, B. Hughes, Aerosol jet printing of electronics: an enabling technology for wearable devices, 2020 Pan Pac. Microelectron. Symp. Pan Pac. 2020 (2020), https://doi.org/10.23919/PanPacific48324.2020.9059444
[31] Q. Jing, A. Pace, L. Ives, A. Husmann, N. Ćatić, V. Khanduja, J. Cama, S. Kar-Narayan, Aerosol-jet-printed, conformable microfluidic force sensors, Cell Rep. Phys. Sci. 2 (2021) 100386, https://doi.org/10.1016/j.xcrp.2021.100386
[32] Y. Gu, D. Park, S. Gonya, J. Jendrisak, S. Das, D.R. Hines, Direct-write printed broadband inductors, Addit. Manuf. 30 (2019) 100843, https://doi.org/10.1016/j.addma.2019.100843
[33] T.S. Tran, N.K. Dutta, N.R. Choudhury, Graphene inks for printed flexible electronics: graphene dispersions, ink formulations, printing techniques and applications, Adv. Colloid Interface Sci. 261 (2018) 41–61, https://doi.org/10.1016/j.cis.2018.09.003
[34] K. Pan, Y. Fan, T. Leng, J. Li, Z. Xin, J. Zhang, L. Hao, J. Gallop, K.S. Novoselov, Z. Hu, Sustainable production of highly conductive multilayer graphene ink for wireless connectivity and IoT applications, Nat. Commun. 9 (2018) 5197, https://doi.org/10.1038/s41467-018-07632-w
[35] D.S. Saidina, N. Eawwiboonthanakit, M. Mariatti, S. Fontana, C. Hérold, Recent development of graphene-based ink and other conductive material-based inks for flexible electronics, J. Electron. Mater. 48 (2019) 3428–3450, https://doi.org/10.1007/s11664-019-07183-w
[36] M.K. Aslam, Y. Niu, M. Xu, MXenes for non-lithium-ion (Na, K, Ca, Mg, and Al) batteries and supercapacitors, Adv. Energy Mater. 11 (2021) 2000681, https://doi.org/10.1002/aenm.202000681
[37] F. Bu, M.M. Zagho, Y. Ibrahim, B. Ma, A. Elzatahry, D. Zhao, Porous MXenes: synthesis, structures, and applications, Nano Today 30 (2020) 100803, https://doi.org/10.1016/j.nantod.2019.100803
[38] F. Shahzad, S.A. Zaidi, R.A. Naqvi, 2D Transition metal carbides (MXene) for electrochemical sensing: a review, Crit. Rev. Anal. Chem. (2020) 1–17, https://doi.org/10.1080/10408347.2020.1836470
[39] M. Mariano, O. Mashtalir, F.Q. Antonio, W.H. Ryu, B. Deng, F. Xia, Y. Gogotsi, A.D. Taylor, Solution-processed titanium carbide MXene films examined as highly transparent conductors, Nanoscale 8 (2016) 16371–16378, https://doi.org/10.1039/c6nr03682a
[40] J. Zhang, S. Li, S. Hu, Y. Zhou, Chemical stability of Ti3C2 MXene with Al in the temperature range 500–700 °C, Mater. (Basel) 11 (2018) 1–9, https://doi.org/10.3390/ma11101979
[41] Y. Zhang, K. Chen, Y. Li, J. Lan, B. Yan, L. Shi, R. Ran, High-strength, self-healable, temperature-sensitive, MXene-containing composite hydrogel as a smart compression sensor, ACS Appl. Mater. Interfaces 11 (2019) 47350–47357, https://doi.org/10.1021/acsami.9b16078
[42] N. Jaya Prakash, B. Kandasubramanian, Nanocomposites of MXene for industrial applications, J. Alloy. Compd. 862 (2021) 158547, https://doi.org/10.1016/j.jallcom.2020.158547
[43] J.-C. Lei, X. Zhang, Z. Zhou, Recent advances in MXene: preparation, properties, and applications, Front. Phys. 10 (2015) 276–286, https://doi.org/10.1007/s11467-015-0493-x
[44] K. Kannan, K.K.K.K. Sadasivuni, A.M.A.M. Abdullah, B. Kumar, Current trends in MXene-based nanomaterials for energy storage and conversion system: a mini review, Catalysts 10 (2020) 1–28, https://doi.org/10.3390/catal10050495
[45] C.J. Zhang, V. Nicolosi, Graphene and MXene-based transparent conductive electrodes and supercapacitors, Energy Storage Mater. 16 (2019) 102–125, https://doi.org/10.1016/j.ensm.2018.05.003
[46] M. Wu, M. He, Q. Hu, Q. Wu, G. Sun, L. Xie, Z. Zhang, Z. Zhu, A. Zhou, Ti3C2 MXene-based sensors with high selectivity for NH3 detection at room temperature, ACS Sens. 4 (2019) 2763–2770, https://doi.org/10.1021/acssensors.9b01308
[47] M. Xin, J. Li, Z. Ma, L. Pan, Y. Shi, MXenes and their applications in wearable sensors, Front. Chem. 8 (2020) 1–14, https://doi.org/10.3389/fchem.2020.00297
[48] A. Sinha, Dhanjai, H. Zhao, Y. Huang, X. Lu, J. Chen, R. Jain, MXene: an emerging material for sensing and biosensing, TrAC - Trends Anal. Chem. 105 (2018) 424–435, https://doi.org/10.1016/j.trac.2018.05.021
[49] Z. Cao, Y. Yang, Y. Zheng, W. Wu, F. Xu, R. Wang, J. Sun, Highly flexible and sensitive temperature sensors based on Ti3C2T: x (MXene) for electronic skin, J. Mater. Chem. A 7 (2019) 25314–25323, https://doi.org/10.1039/c9ta09225k
[50] Y. Wang, M. Mehrali, Y.Z. Zhang, M.A. Timmerman, B.A. Boukamp, P.Y. Xu, J.E. ten Elshof, Tunable capacitance in all-inkjet-printed nanosheet heterostructures, Energy Storage Mater. 36 (2021) 318–325, https://doi.org/10.1016/j.ensm.2021.01.009
[51] C. (John) Zhang, L. McKeon, M.P. Kremer, S.H. Park, O. Ronan, A. Seral-Ascaso, S. Barwich, C. Coileáin, N. McEvoy, H.C. Nerl, B. Anasori, J.N. Coleman, Y. Gogotsi, V. Nicolosi, Additive-free MXene inks and direct printing of micro-supercapacitors, Nat. Commun. 10 (2019) 1–9, https://doi.org/10.1038/s41467-019-09398-1
[52] M. Smith, Y.S. Choi, C. Boughey, S. Kar-Narayan, Controlling and assessing the quality of aerosol jet printed features for large area and flexible electronics, Flex. Print. Electron. 2 (2017) 015004, https://doi.org/10.1088/2058-8585/aa5af9
[53] Y.Z.Y.-Z. Zhang, Y. Wang, Q. Jiang, J.K.J.K. El-Demellawi, H. Kim, H.N.H.N. Alshareef, MXene printing and patterned coating for device applications, Adv. Mater. 32 (2020) 1–26, https://doi.org/10.1002/adma.201908486
[54] A. Saleh, S. Wustoni, E. Bihar, J.K. El-Demellawi, Y. Zhang, A. Hama, V. Druet, A. Yudhanto, G. Lubineau, H.N. Alshareef, S. Inal, Inkjet-printed $Ti_3C_2T_x$ MXene electrodes for multimodal cutaneous biosensing, J. Phys. Mater. 3 (2020) 044004, https://doi.org/10.1088/2515-7639/abb361

Michela Borghetti received the master's degree cum laude, in electronic engineering from the University of Brescia in 2012. In 2015, she was a visiting Ph.D. student at Universitat Politècnica de Catalunya. In 2016, she received the Ph.D. in Technology for Health from the University of Brescia. She is currently Postdoctoral Researcher with the Department of Information Engineering, University of Brescia. Her research is focused on the design and fabrication of sensors for healthcare using innovative printing technologies.

Mauro Serpelloni received his M.Sc. degree in Management Engineering and Ph.D. in electronic instrumentation from the University of Brescia in 2003 and 2006, respectively. Since 2010 he is Associate Professor with the Department of Information Engineering, University of Brescia. His research interests include electronic instrumentation, sensors, contactless transmissions between sensors and electronics and signal processing for microelectromechanical systems. Recently, research has been addressed to the development of wearable sensors, autonomous sensors for biomedical applications and devices implantable inside the human body. He is manager of a new laboratory for aerosol jet printing.

Emilio Sardini graduated in 1983 in Electronic Engineering from the Polytechnic of Milan. Since 1984 he conducts its research and teaching activities at the Department of Electronics for Automation, University of Brescia. Since 2006 he is full professor of Electrical and Electronic Measurement. He has done intensive research in the field of electronic instrumentation, sensors, and signal conditioning electronics. Recently, research has been addressed to the development of autonomous sensors for biomedical applications with some specific interest toward devices implantable inside the human body. He is author or coauthor of more than one hundred papers published on international journal.

Dahnan Spurling is an Irish Research Council and Intel EPS PhD candidate under the supervision of Prof. Valeria Nicolosi in Trinity College Dublin. Research is focused on the synthesis and deposition of MXenes for electronics, energy storage, and biomedical applications using a variety of conventional and additive manufacturing techniques.

Valeria Nicolosi is the Chair of Nanomaterials and Advanced Microscopy at the School of Chemistry in Trinity College Dublin (TCD).She received a BSc (Hons) in Industrial Chemistry from the University of Catania (Italy) and a Ph.D. in Physics from the University of Dublin, Trinity College in 2006. She moved to the University of Oxford in February 2008 as a Marie Curie Fellow, to work in the field of advanced electron microscopy. In April 2008 she was awarded with a Royal Academy of Engineering/EPSRC Fellowship. In 2012 she returned to Trinity College Dublin as an ERC Research Professor. In 2016 she was promoted to Chair of Nanomaterials and Advanced Microscopy. She is the first woman to have reached the position of Chair in the School of Chemistry since the foundation of Trinity College Dublin in 1592.In 2018, 2019 and 2020 she was recognized as one of the world's most influential researchers of the past decade, demonstrated by the production of multiple highly-cited papers that rank in the top 1% by citations for field and year in Web of Science.She has won numerous awards: the RDS/Intel Prize for Nanoscience 2012, the World Economic Forum Young Scientist 2013, EU Woman in Technology Award 2013, SFI President of Ireland Young Researcher Award 2014, SFI Irish Early Stage Researcher 2016, TCD ERC Awardee 2017, Women Business Forum Women of the Decade in Science & Innovation 20.